RSC Advances

ROYAL SOCIETY OF CHEMISTRY

www.rsc.org/advances

Graphical Abstract

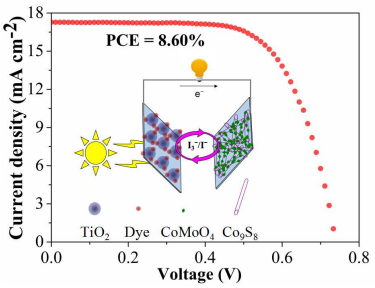

The efficiency of DSSCs with $CoMoO_4/Co_9S_8$ CEs was 8.60% under the light intensity of 100 mW cm^{-2} (AM 1.5 G).

Hydrothermal synthesis of $CoMoO_4/Co_9S_8$ hybrid nanotubes based on counter electrodes for high efficient dye-sensitized solar Cells

Jinghao Huo, Jihuai Wu*, Min Zheng, Yongguang Tu, Zhang Lan

Engineering Research Center of Environment-Friendly Functional Materials, Ministry of Education, Institute of Materials Physical Chemistry, Huaqiao University, Quanzhou 362021, China

Abstract: The $CoMoO_4/Co_9S_8$ hybrid nanotubes are fabricated by a simple two-step hydrothermal method, which was similar with preparing Co_9S_8 nanotubes. Then $CoMoO_4/Co_9S_8$ nanotubes are coated on a fluorine-doped tin oxide glass to fabricate a counter electrode (CE) by spin-casting. Field emission scanning electron microscopy images show that the introduction of $CoMoO_4$ to Co_9S_8 makes the surface of $CoMoO_4/Co_9S_8$ nanotubes rougher. The cyclic voltammetry shows that the electrocatalytic activity of $CoMoO_4/Co_9S_8$ CE is similar with Pt CE when the $(NH_4)_2MoO_4$ content was 60 wt%. Meanwhile the electrochemical impedance spectroscopy and Tafel measurements demonstrate that the $CoMoO_4/Co_9S_8$ CE had smaller values of R_s and R_{ct} than that of Pt CE. The dye-sensitized solar cells assembled with $CoMoO_4/Co_9S_8$ CE obtain excellent values of open-circuit voltage (0.743 V), short-circuit current density (17.276 mA cm^{-2}), fill factor (0.670) and a wonderful power conversion efficiency (8.60%), which is higher than that of DSSCs with Co_9S_8 CE (7.69%) or Pt CE (8.13%) under the light intensity of 100 mW cm^{-2} (AM 1.5 G).

* Corresponding author. Tel.: +86 595 22693899; fax: +86 595 22692229.

E-mail address: jhwu@hqu.edu.cn (J. Wu).

Keywords: dye-sensitized solar cells, counter electrode, $CoMoO_4$, Co_9S_8, nanotubes

1. Introduction

Dye-sensitized solar cells (DSSCs) are a type of clean, low-cost and easily-fabricated equipment to convert solar energy into electricity [1-3]. Today many researchers try their best to explore the cheap and high efficient materials to fabricate DSSCs. In general, a DSSC includes three parts: a dye-sensitized photoanode (typically, TiO_2), an electrolyte (typically, I_3^-/I^-), and a counter electrode (CE). The role of CEs is to collect the electrons from photoanode by the external circuit and has a catalytic reaction for the reduction of I_3^-/I^- [3]. The metal of platinum is one of the most commonly used materials for CEs, while the characteristics of exorbitant price and easy corrosion limit its application [4]. Nowadays many other materials are as the candidate materials to fabricate the CEs of DSSCs, such as carbon materials [5-7], conducting polymers [8-10], alloys [11, 12], metal -oxide [13], -nitride [14], -sulfide [15, 16], -selenide [17, 18], -phosphide [19] and hybrid materials [20-22].

Cobalt sulfide is one kind of transition metal sulfide catalytic materials and it includes a variety of binary sulfides, such as CoS, CoS_2, Co_3S_4 Co_9S_8 and so on [23]. Among these cobalt sulfides, Co_9S_8 has attracted intense interest because of the complicated structure, interesting properties. Hence Co_9S_8 was widely employed in hydrogenation and hydrodesulfurization [24], cathodic material for lithium batteries [25, 26], supercapacitors [27, 28] and other fields [29]. Based on its good catalytic activity, some researchers synthesized Co_9S_8 to be CE materials of DSSCs. In 2013, Chang et. al [30] prepared a Co_9S_8 nanocrystal ink by spray-deposited and the large area DSSCs with this Co_9S_8 CE obtained a power conversion efficiency (PCE) of 7.02 ± 0.18%, which was similar to that of DSSC with Pt CE (7.2 ± 0.12%). Chen et. al [31]

fabricated a novel one-dimensional Co_9S_8 acicular nanotube arrays (ANTAs) on a conducting plastic substrate by a two-step approach. With this Co_9S_8 ANTAs as CEs, the DSSCs achieved a PCE of 5.47%, which was comparable to that of the DSSC using sputtered Pt (5.62%). In addition, $CoMoO_4$ attracted researchers' attention due to its advantages of low cost, non-toxic, and exhibits enhanced electrochemical properties on lithium batteries [32] and supercapacitors [33, 34].

In this paper, $CoMoO_4/Co_9S_8$ hybrid nanotubes were synthesized by a two-step hydrothermal method. In the first step, $Co(CO_3)_{0.35}Cl_{0.20}(OH)_{1.10}$ nanoneedles were fabricated and used to be the templates of fabricating $CoMoO_4/Co_9S_8$ hybrid nanotubes [35]. The as-obtained hybrids could take advantage of the favorable property of $CoMoO_4$ and Co_9S_8. Cyclic voltammetry (CV), electrochemical impedance spectroscopy (EIS) and Tafel tests proved that the $CoMoO_4/Co_9S_8$ CEs possessed good conductivity and catalytic activity for the reduction of I_3^-/I^-. With $CoMoO_4/Co_9S_8$ hybrid nanotubes as CEs, the DSSCs had a high current density (17.276 mA cm^{-2}) and an excellent PCE of 8.60%, which was higher than that of DSSCs with Pt CE (8.13%).

2. Experimental

2.1. Chemicals and materials

The cobalt chloride hexahydrate ($CoCl_2 \cdot 6H_2O$, ≥99%), urea (≥99.0%), sodium sulfide nonahydrate ($Na_2S \cdot 9H_2O$, ≥98%), isopropyl alcohol (IPA, ≥99.7%), titanium tetrachloride ($TiCl_4$, 99.9%), acetonitrile (ACN, 99.9%), tetraethyl ammonium iodide (98%), tetrabutyl ammonium iodide (99%), tetramethyl ammonium iodide (99%), 4-tert-butyl pyridine (tBP, 96%), lithium perchlorate ($LiClO_4$, 99.9%), sodium iodide (NaI, >99%), potassium iodide (KI, 99%), lithium iodide (LiI, 99.5%), and iodine (I_2, 99%) were all A. R. grade and purchased from Sinopharm Chemical Reagent Co. Ltd,

China. Ammonium molybdate ($(NH_4)_2MoO_4$, 99.99%) was purchased from Alfa Aesar. N719 dye (Ru[LL'-$(NCS)_2$], L = 2, 2'-bipyridyl-4, 4'-dicarboxylic acid, L' = 2, 2'-bipyridyl-4, 4'-ditetrabutylammonium carboxylate) was acquired from Dye sol.

The fluorine-doped tin oxide (FTO) glass (14 Ω sq^{-1}) was purchased from Wuhan Lattice Solar Energy Technology Co. Ltd, China. The FTO glass was cut into pieces (1.5×1.5 cm^2) and washed with cleaner, acetone and IPA in turn and stored in anhydrous ethanol.

2.2. Synthesis of $CoMoO_4/Co_9S_8$ hybrid nanotubes

Scheme 1 here

The $CoMoO_4/Co_9S_8$ hybrid nanotubes were fabricated by the same two-step hydrothermal method as that of Co_9S_8 (scheme 1). First, to prepare a precursor of $Co(CO)_{0.35}Cl_{0.20}(OH)_{1.10}\cdot 1.74H_2O$ nanorods with $CoCl_2\cdot 6H_2O$ and urea. In brief, 10 mmol of $CoCl_2\cdot 6H_2O$ and 10 mmol of urea were added into 60 mL deionized water under intense stirring. Then the solution was stirred for 10 minutes and transferred to a 100 mL Teflon-lined stainless steel autoclave, heated in an oven at 130 ˚C for 10 h. After natural cooling to room temperature, the underlying precipitation was washed with deionized water and anhydrous ethanol three times respectively and dried in vacuum at 60 ˚C for 24 h and the precursor powder was obtained.

Followed by a hydrothermal process with $(NH_4)_2MoO_4$ and $Na_2S\cdot 9H_2O$, the precursor was transformed into $CoMoO_4/Co_9S_8$ hybrid nanotubes. In a 100 mL Teflon-lined stainless steel autoclave, the solution with 400 mg of precursor and 1.2 g of $Na_2S\cdot 9H_2O$ and $(NH_4)_2MoO_4$ (60 wt%) were mixed with 60 mL deionized water under intense stirring for 10 minutes and then heated at 180 ˚C for 8 h. After natural cooling to room temperature, the as-product of $CoMoO_4/Co_9S_8$ nanotubes was washed with deionized water and anhydrous ethanol and dried in a vacuum oven at 60 ˚C for

24 h. For comparison, the pure Co_9S_8 was synthesized by the same method without the addition of $(NH_4)_2MoO_4$. And the effect of different contents (20, 40, 60, 80 wt%) of $(NH_4)_2MoO_4$ on the performance of CEs was studied and the relevant $CoMoO_4/Co_9S_8$ nanotubes were marked $CoMoO_4/Co_9S_8$-x (x = the contents of $(NH_4)_2MoO_4$, x wt%)

2.3. Preparation of $CoMoO_4/Co_9S_8$ counter electrodes

The $CoMoO_4/Co_9S_8$ CE was prepared by a spin-casting method. Typically, 100 mg as-product of $CoMoO_4/Co_9S_8$ was added into 10 mL IPA and sonicated for 20 mins. Then the solution was coated on FTO glass by spin-casting for three times at a rate of 4000 rpms for 20 seconds. After every time spin-casting, the FTO substrate was thermally treated at 80 ˚C for 10 mins and then the next layer was coated. The Co_9S_8 CE was fabricated with the same method.

2.4. Fabrication of DSSCs

TiO_2 photoanodes consisted of a ~160 nm TiO_2 under layer, a 12 μm TiO_2 nanocrystalline layer and a scattering layer treating with $TiCl_4$ solution. After sensitized with a 0.3 mM N719 dye ethanol solution for 24 h, the TiO_2 photoanodes absorbed N719 dye were fabricated. In addition, the active areas of photoanodes were about 0.3×0.4 cm^2. A DSSC was a sandwich structure assembled with a attaching dye sensitized TiO_2 photoanode, a CE and a I_3^-/I^- electrolyte between them and employed in having photocurrent-photovoltage (J-V) tests. In a DSSC, cyanoacrylate adhesive was used to adhere these two electrodes together and a vacuum pump was used to inject electrolytes into the cell internal space. The I_3^-/I^- electrolyte was prepared by adding tetraethyl ammonium iodide (0.1 M), tetrabutyl ammonium iodide (0.1 M), tetramethyl ammonium iodide (0.1 M), NaI (0.1 M), KI (0.1 M), LiI (0.1 M), I_2 (0.05 M), and tBP (0.5 M) into an ACN solution. And a Pt CE (2.5×2 cm^2, prepared by

magnetron sputtering, Wuhan Lattice Solar Energy Technology Co. Ltd, China) was used to be a comparison. A traditional symmetrical cell (CE/electrolyte/CE) was assembled by two identical CEs and used to have electrochemical impedance spectroscopy (EIS) and Tafel tests.

2.5. Characterizations and measurements

The crystal structures of Co_9S_8 and $CoMoO_4/Co_9S_8$ were obtained by an X-ray Diffraction (XRD, Bruker D8,Cu Kα, λ=1.5418 Å) at a scan rate of 5° min^{-1}. The composition of $CoMoO_4/Co_9S_8$ was measured by X-ray photoelectron spectroscopy (XPS, ESCALAB 250XI, Thermo). XPS was performed by using Al K_α (hν = 1486.6 eV) with power of 150 W and beam spot of 500 μm. The XPS data were calibrated by C1s (284.8 eV) and fitted by the XPSPEAK 4.0 software. The surface Morphologies of as-prepared products were performed by field emission scanning electron microscopy (FESEM, SU8010, HITACHI) and the energy-dispersive X-ray (EDX) spectroscopy was used to investigate the element distribution and element types of $CoMoO_4/Co_9S_8$-60.

The electrochemical properties of CEs were studied by cyclic voltammetry (CV), EIS and Tafel tests with an electrochemical working station (IM6, Zahner, Germany). CV tests were used to study the electrocatalytic ability of CEs for I_3^-/I^- by a three-electrode cell, in which a as-prepared CE was a work electrode, a Pt sheet was used as CE and an Ag/AgCl was a reference electrode. Meanwhile the tests were performed in an ACN solution of 10 mM LiI, 1 mM I_2, and 100 mM $LiClO_4$ from -0.4 V to 1.4 V with a scan rate of 50 mV s^{-1}. EIS measurement was conducted in dark condition and the frequency range was from 100 kHz to 100 mHz under bias voltage of 0 V and the corresponding amplitude of 5 mV. And the ZsimpWin software was used to fit the EIS data. Tafel curves were carried out with a voltage range from 1 V to

1 V and at a scan rate of 10 mV s^{-1}.

J-V tests of DSSCs were performed under simulated solar illumination of 100 mW cm^{-2} (AM 1.5 G) with a solar simulator (PVIV-94043A, Newport, USA) and a 450W xenon lamp as light source. All the tests were performed five times and the average data were taken.

3. Results and discussion

3.1. Morphology and compositions of CEs

Figure 1 here

Fig. 1 shows the XRD patterns of the as-prepared Co_9S_8, $CoMoO_4$ and $CoMoO_4/Co_9S_8$-60. The as-prepared $CoMoO_4$ in the absence of Na_2S has obvious diffraction peaks, which were assigned to the planes of $CoMoO_4$ (JCPDS 021-0868). Meanwhile, the Co9S8 and $CoMoO_4/Co_9S_8$-60 both have the same diffraction peaks as the planes of Co_9S_8 (JCPDS 65-1765). While there are some other small peaks could be detected in the XRD pattern of $CoMoO_4/Co_9S_8$-60 and they can be well indexed to $CoMoO_4$. This indicted that the resulting product was a hybrid material of $CoMoO_4$ and Co_9S_8, which was prepared with 60 wt% $(NH_4)_2MoO_4$ in the second hydrothermal process.

Figure 2 here

To further research the chemical compositions and the element valence of $CoMoO_4/Co_9S_8$-60 CE, XPS was employed in the study and the data were recorded in Fig. 2. Fig. 2a shows the survey scan of $CoMoO_4/Co_9S_8$ CE, which illustrated the presence of Co, O, Mo and S. Fig. 2b is the high resolution scan of the Mo 3d peak and there is one characteristic doublet of hexavalent molybdenum of Mo 3d at 235.9 and 232.8 eV, which correspond to Mo $3d_{3/2}$ and Mo $3d_{5/2}$ orbitals, respectively [36]. Fig. 2c shows the high resolution scan of Co $2p_{3/2}$ region and there are two obvious

peaks at 780.4 eV and 778.4 eV belong to Co^{2+} and Co_9S_8 [34, 37]. Fig. 2d shows the core level spectra of S 2p and there are two characteristic doublet of Co_9S_8 at 161.4 and 162.5 eV which correspond to S $2p_{3/2}$ and S $2p_{1/2}$, respectively [37].

Figure 3 here

Fig. 3 is the FESEM and EDX images of the surface morphology of as prepared materials. Fig. 3a shows surface morphology of precursor $(Co(CO)_{0.35}Cl_{0.20}(OH)_{1.10}\cdot 1.74H_2O)$, which consists of many nanorods (~200 nm in diameters, and lengths of several micrometers in lengths). After a hydrothermal process of precursor and $Na_2S\cdot 9H_2O$, the as-prepared product of Co_9S_8 was transformed into nanotubes with smooth surface (Fig. 3b). While the adding of $(NH_4)_2MoO_4$ in the second hydrothermal process could change the surface morphology of $CoMoO_4/Co_9S_8$. $CoMoO_4/Co_9S_8$-40 hybrid consisted of some nanotubes and some sheets (Fig. 3c). With the increasing of $(NH_4)_2MoO_4$ content to 60 wt%, the length of Co_9S_8 nanotubes was increased and the surface was rougher with $CoMoO_4$ nanosheets (Fig. 3d), and this rough surface topography was beneficial to improve the contact of CE and electrolyte and the catalytic activity for the reduction of I_3^- to I^-. When the $(NH_4)_2MoO_4$ content was 80 wt%, the length of nanotubes of $CoMoO_4/Co_9S_8$-80 turned into short and there are many lumps (Fig. 3e). Furthermore, $CoMoO_4/Co_9S_8$-90 hybrid was fabricated with layered materials which get together and some nanotubes was attached on the surface of them (Fig. 3f). Fig. 3g is the element mapping of $CoMoO_4/Co_9S_8$-60, which Co and S were uniformly distributed in the nanotubes and Mo was distributed in the sheets of the nanotubes surface. Fig. 3h is the EDX spectroscopy confirmed that the composite of $CoMoO_4/Co_9S_8$-60 consisted of four elements (Co, Mo, O, S).

The formation mechanism of the Co_9S_8 nanotubes can be illustrated by

Kirkendall effect [37, 38]. In the first hydrothermal process, urea could hydrolyze to yield OH^- and CO_3^{2-} in the solution, and the OH^-, CO_3^{2-} and Cl- had a reaction with Co^{2+} to form $Co(CO)_{0.35}Cl_{0.20}(OH)_{1.10}$ precipitation (Eqs. (1)-(4)) [39].

$$H_2NCONH_2 + H_2O \rightarrow 2NH_3 + CO_2 \quad (1)$$

$$NH_3 + H_2O \rightarrow NH_4^+ + OH^- \quad (2)$$

$$CO_2 + H_2O \rightarrow CO_3^{2-} + 2H^- \quad (3)$$

$$Co^{2+} + 0.35CO_3^{2-} + 0.20Cl^- + 1.10OH^- \rightarrow Co(CO_3)_{0.35}Cl_{0.20}(OH)_{1.10} \quad (4)$$

In the second step, the as-prepared $Co(CO)_{0.35}Cl_{0.20}(OH)_{1.10}$ reacted with Na_2S and $(NH_4)_2MoO_4$ to fabricate Co_9S_8 nanotubes and $CoMoO_4$ nanosheets on their surface. Firstly, on the surfaces of nanorods, S^{2-} ions and $Co(CO)_{0.35}Cl_{0.20}(OH)_{1.10}$ nanorods react to form a thin layer of Co_9S_8 nanocrystallites, which contain many grain boundaries to the benefit of the diffusion and reaction of materials through the Co_9S_8 layer. According to Kirkendall effect, the different diffusivities of the different components finally lead to form tubular structures. Meanwhile, the hydrolyzation of $(NH_4)_2MoO_4$ can be expressed as Eqs. (5), and the MoO_4^{2-} ions would react with $Co(CO)_{0.35}Cl_{0.20}(OH)_{1.10}$ to fabricate $CoMoO_4$ on the surface of Co_9S_8 nanotubes.

$$(NH_4)_2MoO_4 \rightarrow 2NH_4^+ + MoO_4^{2-} \quad (5)$$

3.2. Electrochemical properties of CEs

Figure 4 here

In order to evaluate the electrochemical property of $CoMoO_4/Co_9S_8$ CEs and have a comparison with Pt CE, the CV, EIS and Tafel measurements were employed. Fig. S1 shows the effect of $(NH_4)_2MoO_4$ content for the CV of CEs and the absolute values of over potentials (ΔE) and cathodic current density ($J_{Red\text{-}1}$) in left pair of peaks

were recorded in table S1. The values of ΔE and J_{Red-1} are two important factors to investigate the electrocatalytic activity of CEs for I_3^-/I^-. Smaller ΔE and higher values of J_{Red-1} indicate the CEs had an excellent electrocatalytic activity. The similar shapes of CV curves indicated these CEs have similar electrocatalytic activity. With the increasing of $(NH_4)_2MoO_4$ content, the electrocatalytic activity was improved. When the $(NH_4)_2MoO_4$ content increased to 60 wt%, the value of ΔE was the small and the value of J_{Red-1} was the highest. However, further increase the $(NH_4)_2MoO_4$ content, the value of ΔE was increased and J_{Red-1} was decreased. The reason maybe that the number of $CoMoO_4$ sheets was increased and had an aggregation with more contents $(NH_4)_2MoO_4$ in the second hydrothermal process. This greatly prevents the the contact of CE and electrolyte and limits the electronic transmission from CEs to electrolyte, hence the electrocatalytic activity of CEs was decreased. Fig. 4 shows the cyclic voltammograms of $CoMoO_4$, Co_9S_8, $CoMoO_4/Co_9S_8$-60 and Pt CEs. Though the shapes of CV curves are similar, the $CoMoO_4/Co_9S_8$ CE has a larger J_{Red-1} and smaller ΔE than that of pure Co_9S_8 CE. Compared to Pt CE, the $CoMoO_4/Co_9S_8$-60 CE has a smaller value of E_{pp} (0.402 V) and a numerical equivalent J_{Red-1} (0.931 mA cm^{-2}) (table 1). The result showed fully that the introduction of $CoMoO_4$ to Co_9S_8 CE could increase the electrocatalytic activity of CE, which was comparable with Pt CE.

Figure 5 here

Table 1 here

Fig. 5 shows the Nyquist plots of the symmetric cells with Co_9S_8, $CoMoO_4/Co_9S_8$-60 and Pt CEs. The inset is the equivalent circuit and the relevant

values are summarized in table 1. There are two semicircles and the high-frequency intercept of the left semicircle on the real axis represents the series resistance (R_s). And the left semicircle is related to the charge-transfer resistance (R_{ct}) at the CE/electrolyte interface, which reflects the catalytic activity of different CEs on the reduction of I_3^- to I^-. Fig. S2 shows the EIS of the symmetric cells with CEs prepared by different $(NH_4)_2MoO_4$ content and the values of R_s and R_{ct} were recorded in table S1. Among these CEs, the $CoMoO_4/Co_9S_8$ CE with 60 wt% $(NH_4)_2MoO_4$ exhibited smallest values of R_s and R_{ct} which indicated that this CE has excellent conductivity and electrocatalytic properties. In Fig. 5, the R_s of the symmetric cells with $CoMoO_4/Co_9S_8$-60 CE is smaller than that of cells with Co_9S_8 CE, which is caused by the introduction of $CoMoO_4$ to Co_9S_8 and then increased the stronger adhesion of $CoMoO_4/Co_9S_8$-60 on FTO. Meanwhile, the value of R_{ct} for the symmetric cells with $CoMoO_4/Co_9S_8$-60 CE is 2.29 Ω cm^2, which is smaller than that of cells with Co_9S_8 CE (9.52 Ω cm^2) and Pt CE (5.21 Ω cm^2). It can be observed that this result is agreed with the data of CV. The small R_s and R_{ct} made the DSSCs with $CoMoO_4/Co_9S_8$-60 CE have high J_{sc} and FF.

Figure 6 here

Tafel polarization was used to further elucidate the catalytic activity of CEs in Fig. 6 and Fig. S3. Tafel curves described the relationship between overpotential and current density and given the information about the exchange current density (J_0), which is the slope in the anodic or cathodic branch. A larger value of J_0 means that the CE has a better electrocatalytic activity for the reduction of I_3^-/I^-. Fig. S3 shows the

Tafel curves of the symmetric cells with CEs prepared by different $(NH_4)_2MoO_4$ content. Among these CEs, the $CoMoO_4/Co_9S_8$-60 CE exhibited a largest value of J_0, which indicated that this CE has excellent electrocatalytic property. From Fig. 6, the value of J_0 for $CoMoO_4/Co_9S_8$-60 CE is larger than that of Co_9S_8 CE and is similar with that of Pt CE. This means that $CoMoO_4/Co_9S_8$-60 CE has a highest electrocatalytic activity for the reduction of I_3^-/I^- among these three CEs. In addition, the J_0 has a closely positive correlation with R_{ct} as Eqs. (1), which R is the gas constant, T is absolute temperature, n is the electron number involved in the reaction and F is Faraday constant. Hence the result of Tafel is consistent with the EIS result well.

$$J_0 = (RT)/(nFR_{ct}) \quad (1)$$

3.3. Photovoltaic performance of DSSCs

Figure 7 here

Table 2 here

Fig. 7 shows the J-V characteristics of DSSCs assembled by Co_9S_8, $CoMoO_4/Co_9S_8$ prepared with 60 wt% $(NH_4)_2MoO_4$ or Pt CEs and the values of open-circuit voltage (V_{oc}), short-circuit current density (J_{sc}), fill factor (FF) and PCE were summarized in table 2. Compared to Co_9S_8 and Pt CEs, $CoMoO_4/Co_9S_8$ CE made the relevant parameters of DSSCs were the largest: V_{oc} = 0.743 V, J_{sc} = 17.276 mA cm^{-2}, FF = 0.670 and PCE = 8.60%. Fig. S4 was the J-V curves of CEs with different $(NH_4)_2MoO_4$ contents and the relevant parameters were recorded in table S2. The values of V_{oc} for these CEs were similar, and the tendency of J_{sc}, FF and PCE

agree with the tendency of CV, EIS and Tafel.

4. Conclusions

In conclusion, this paper prepared $CoMoO_4/Co_9S_8$ hybrid nanotubes by a simple two-step hydrothermal method. Then this material was coated on FTO glass to fabricate a CE by spin-casting. The addition of $(NH_4)_2MoO_4$ in the second hydrothermal process, not only made the surface of Co_9S_8 nanotubes rougher to have a good contact between $CoMoO_4/Co_9S_8$ CE and electrolyte, and improved the electrochemical property of $CoMoO_4/Co_9S_8$ CE. CV results indicated that the electrocatalytic activity of $CoMoO_4/Co_9S_8$ CE was similar with Pt CE when the $(NH_4)_2MoO_4$ content was 60 wt%. Meanwhile the EIS and Tafel measurements demonstrated that the $CoMoO_4/Co_9S_8$ CE had smaller values of R_s and R_{ct} than that of Pt CE. The DSSCs assembled with $CoMoO_4/Co_9S_8$ CE exhibited excellent photovoltaic property of J_{sc} = 17.276 mA cm^{-2} and PCE = 8.60%, which were higher than that of DSSCs with Pt CE (J_{sc} = 16.504 mA cm^{-2}, PCE = 8.13%). This work used a simple approach to prepare a low-cost and high electrochemical property hybrid material to fabricate a non-Pt CE in DSSCs.

Acknowledgement

The authors gratefully acknowledge the financial supporting by the National Natural Science Foundation of China (Nos. 91422301, U1205112, 21301060, 61306077 and 61474047).

References

[1] B. O'Regan, M. Grätzel, Nature, 353 (1991) 737-740.

[2] A. Hagfeldt, G. Boschloo, L. Sun, L. Kloo, H. Pettersson, Chem. Rev., 110 (2010) 6595-6663.

[3] J. Wu, Z. Lan, J. Lin, M. Huang, Y. Huang, L. Fan, G. Luo, Chem. Rev., 115 (2015) 2136-2173.

[4] E. Olsen, G. Hagen, S. Lindquist, Sol. Energy Mater. Sol. Cells, 63 (2000) 267-273.

[5] G. Li, F. Wang, J. Song, F. Xiong, X. Gao, Electrochim. Acta, 65 (2012) 216-220.

[6] M. Ju, J. Kim, H. Choi, I. Choi, S. Kim, K. Lim, J. Ko, J. Lee, I. Jeon, J. Baek, H. Kim, ACS Nano, 7 (2013) 5243-5250.

[7] J. Balamurugana, A. Pandurangana, R. Thangamuthu, Org. Electron., 14 (2013) 1833-1843.

[8] Q. Tai, B. Chen, F. Guo, S. Xu, H. Hu, B. Sebo, X. Zhao, ACS Nano, 5 (2011) 3795-3799.

[9] J. Wu, Q. Li, L. Fan, Z. Lan, P. Li, J. Lin, S. Hao, J. Power Sources, 181 (2008) 172-176.

[10] H. Tsao, J. Burschka, C. Yi, F. Kessler, M. Nazeeruddin, M. Grätzel, Energy Environ. Sci., 4 (2011) 4921-4924.

[11] Y. Duan, Q. Tang, B. He, R. Li, L. Yu, Nanoscale, 6 (2014) 12601-12608.

[12] Y. Duan, Q. Tang, J. Liu, B. He, L. Yu, Angew. Chem. Int. Ed., 53 (2014) 14569-14574.

[13] M. Wu, X. Lin, A. Hagfeldt, T. Ma, Chem. Commun., 47 (2011) 4535-4537.

[14] J. Song, G. Li, K. Xi, B. Lei, X. Gao, R. Kumar, J. Mater. Chem. A, 2 (2014) 10041-10047.

[15] J. Huo, M. Zheng, Y. Tu, J. Wu, L. Hu, S. Dai, Electrochim. Acta, 159 (2015) 166-173.

[16] Z. Wan, C. Jia, Y. Wang, Nanoscale, 7 (2015) 12737-12742.

[17] J. Jia, J. Wu, Y. Tu, J. Huo, M. Zheng, J. Lin, J. Alloys Compd., 640 (2015) 29-33.

[18] F. Gong, H. Wang, X. Xu, G. Zhou, Z. Wang, J. Am. Chem. Soc., 134 (2012) 10953-10958.

[19] M. Wu, J. Bai, Y. Wang, A. Wang, X. Lin, L. Wang, Y. Shen, Z. Wang, A. Hagfeldt, T. Ma, J. Mater. Chem., 22 (2012) 11121-11127.

[20] J. Huo, J. Wu, M. Zheng, Y. Tu, Z. Lan, J.Power Sources, 293 (2015) 570-576.

[21] J. Ma, W. Shen, C. Li, F. Yu, J. Mater. Chem. A, 3 (2015) 12307-12313.

[22] P. Sudhagar, S. Nagarajan, Y. Lee, D. Song, T. Son, W. Cho, M. Heo, K. Lee, J. Won, Y. Kang, ACS Appl. Mater. Interfaces, 3 (2011) 1838-1843.

[23] P. Grange, B. Delmon, J. Less Common Met., 36 (1974) 353-360.

[24] I. Bezverkhyy, P. Afanasiev, M. Danot, J. Phys. Chem. B, 108 (2004) 7709-7715.

[25] Z. Wang, L. Pan, H. Hu, S. Zhao, CrystEngComm, 12 (2010) 1899-1904.

[26] Y. Zhou, D. Yan, H. Xu, J. Feng, X. Jiang, J. Yue, J. Yang, Y. Qian, Nano Energy, 12 (2015) 528-537.

[27] J. Xu, Q. Wang, X. Wang, Q. Xiang, B. Liang, D. Chen, G. Shen, ACS Nano, 7 (2013) 5453-5426.

[28] R. Ramachandran, M. Saranya, C. Santhosh, V. Velmurugan, B. Raghupathy, S. Jeong, A. Grace, RSC Adv., 4 (2014) 21151-21162.

[29] G. Wang, S. Zhuo, Phys. Chem. Chem. Phys., 15 (2013) 13801-13804.

[30] S. Chang, M. Lu, Y. Tung, H. Tuan, ACS Nano, 7 (2013) 9443-9451.

[31] H. Chen, C. Kung, C. Tseng, T. Wei, N. Sakai, S. Morita, M. Ikegami, T. Miyasaka, K. Ho, J. Mater. Chem. A, 1 (2013) 13759-13768.

[32] T. Yang, H. Zhang, Y. luo, L. Mei, D. Guo, Q. Li, T. Wang, Electrochim. Acta, 158 (2015) 327-332.

[33] D. Guo, H. Zhang, X. Yu, M. Zhang, P. Zhang, Q. Li, T. Wang, J. Mater. Chem. A, 1 (2013) 7247-7254.

[34] X. Xia, W. Lei, Q. Hao, W. Wang, X. Wang, Electrochim. Acta, 99 (2013) 253-261.

[35] J. Pu, Z. Wang, K. Wu, N. Yu, E. Sheng, Phys. Chem. Chem. Phys., 16 (2014) 785-791.

[36] Z. Li, L. Gao, S. Zheng, Mater. Lett., 57 (2003) 4605-4610.

[37] Z. Wang, L. Pan, H. Hu, S. Zhao, CrystEngComm, 12 (2010) 1899-1904.

[38] E. Kirkendall, Trans. AIME, 147 (1942) 107-116.

[39] W. Guo, C. Chen, M. Ye, M. Lv, C. Lin, Nanoscale, 6 (2014) 3656-3663.

Figure and Table Captions

Scheme 1 Schematic diagram of preparing $CoMoO_4/Co_9S_8$ CEs.

Fig. 1 XRD patterns of Co_9S_8, $CoMoO_4$ and $CoMoO_4/Co_9S_8$-60.

Fig. 2 XPS spectra of $CoMoO_4/Co_9S_8$-60 CE: (a) Survey scan, and the high resolution scans: (b) Mo 3d peak, (c) Co $2p_{3/2}$ peak, (d) S 2p peak and their related fittings.

Fig. 3 FESEM images (a) $(Co(CO)_{0.35}Cl_{0.20}(OH)_{1.10}\cdot 1.74H_2O)$, (b) Co_9S_8, (c) $CoMoO_4/Co_9S_8S_8$-40 (d) $CoMoO_4/Co_9S_8S_8$-60, (e) $CoMoO_4/Co_9S_8S_8$-80 and (f) $CoMoO_4/Co_9S_8S_8$-90 and (g) the element distribution mapping images of $CoMoO_4/Co_9S_8$-60, (h) the EDX spectroscopy of $CoMoO_4/Co_9S_8$-60.

Fig. 4 CV curves of CEs: Co_9S_8, $CoMoO_4/Co_9S_8$-60 and Pt CEs at a scan rate of 50 mV s^{-1}.

Fig. 5 EIS curves of Co_9S_8, $CoMoO_4/Co_9S_8$-60 and Pt CEs and the insert is the equivalent circuit diagram.

Fig. 6 Tafel curves of Co_9S_8, $CoMoO_4/Co_9S_8$-60 and Pt CEs.

Fig. 7 J-V curves of the DSSCs based on Co_9S_8, $CoMoO_4/Co_9S_8$-60 and Pt CEs under the light intensity of 100 mW cm^{-2} (AM 1.5 G).

Table 1 CV and EIS data of Co_9S_8, $CoMoO_4/Co_9S_8$-60 and Pt CEs.

Table 2 The photovoltaic data of the DSSCs based on Co_9S_8, $CoMoO_4/Co_9S_8$-60 and Pt CEs.

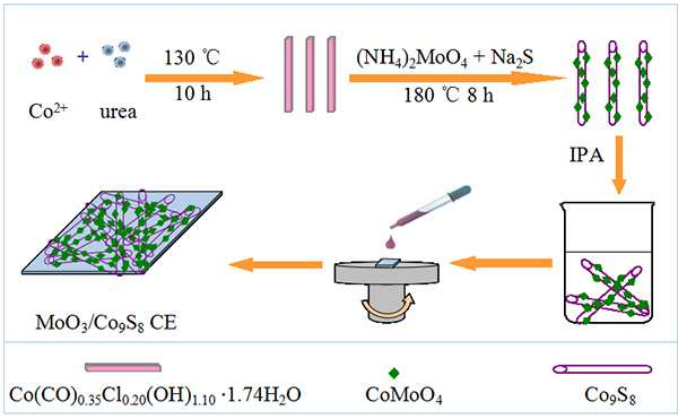

Scheme 1 Schematic diagram of preparing $CoMoO_4/Co_9S_8$ CEs.

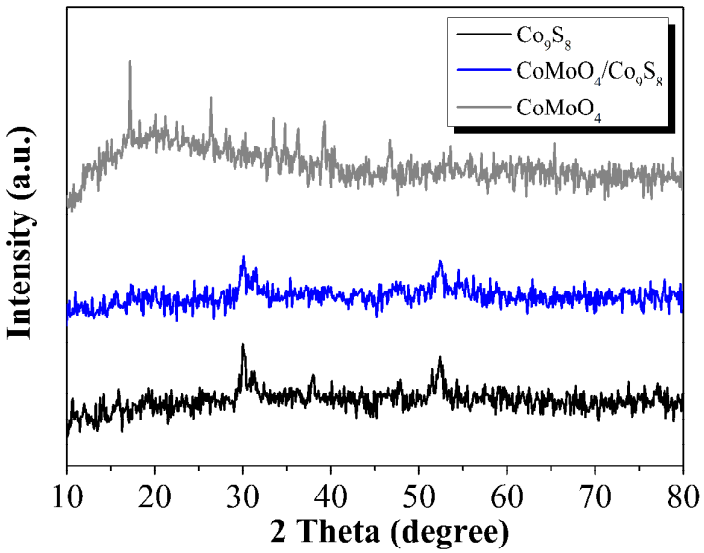

Fig. 1 XRD patterns of Co_9S_8, $CoMoO_4$ and $CoMoO_4/Co_9S_8S_8$-60.

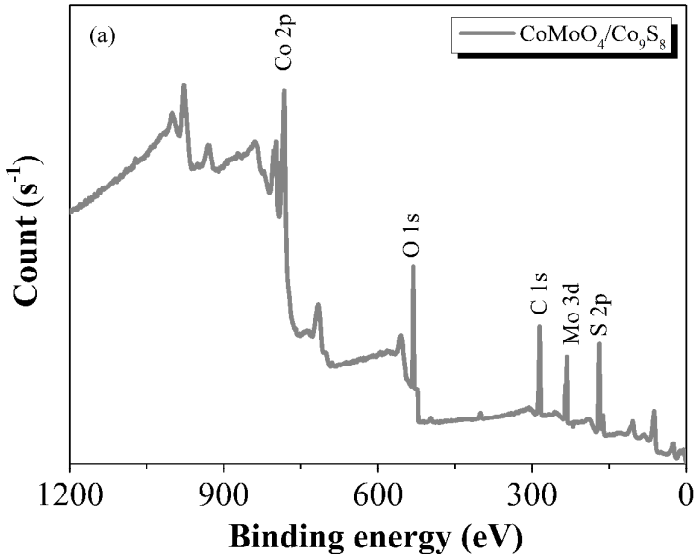

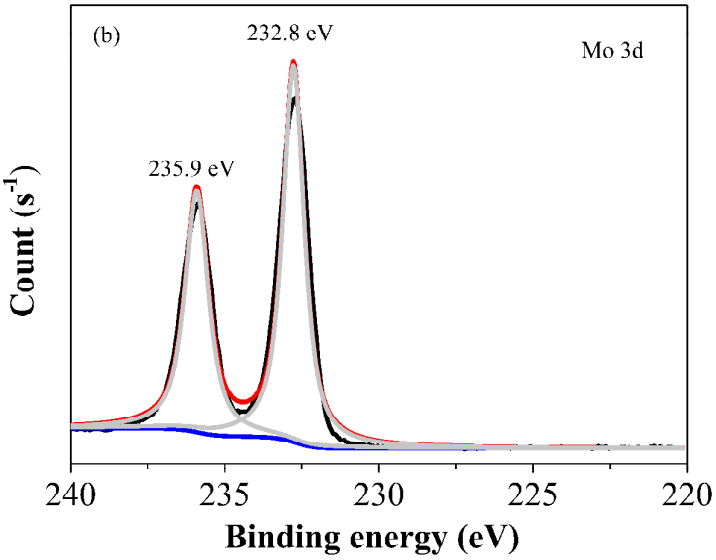

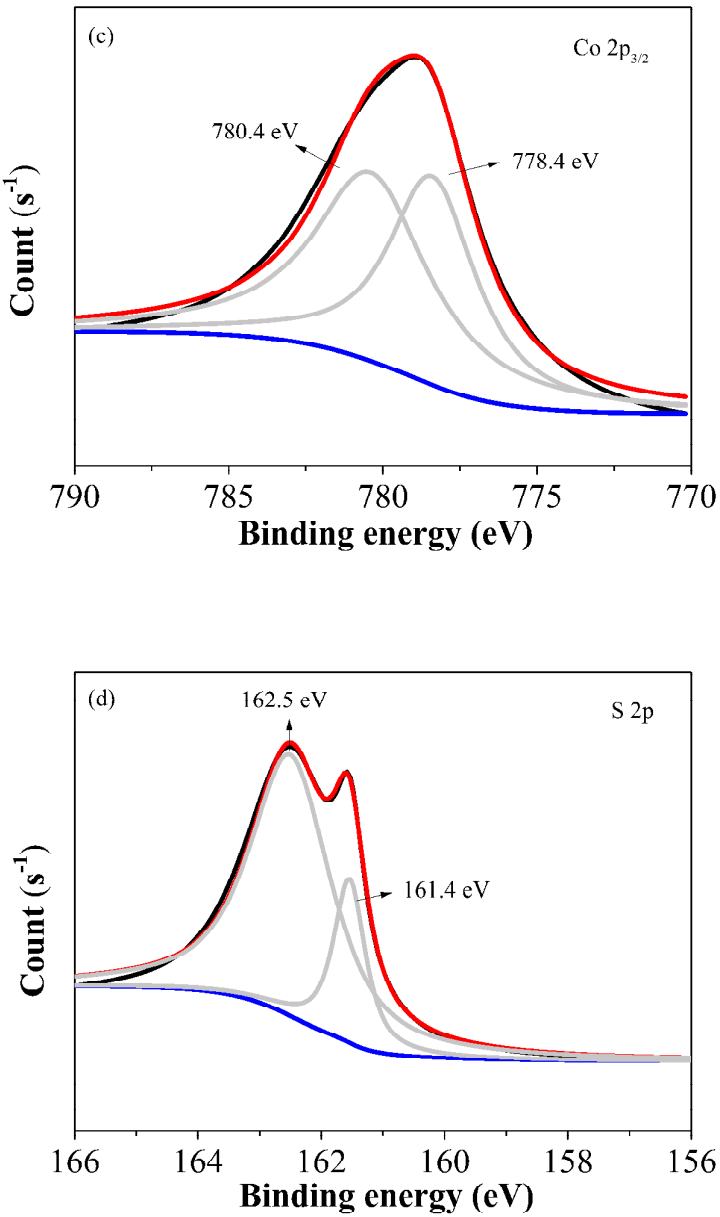

Fig. 2 XPS spectra of $CoMoO_4/Co_9S_8$-60 CE: (a) Survey scan, and the high resolution scans: (b) Mo 3d peak, (c) Co $2p_{3/2}$ peak, (d) S 2p peak and their related fittings.

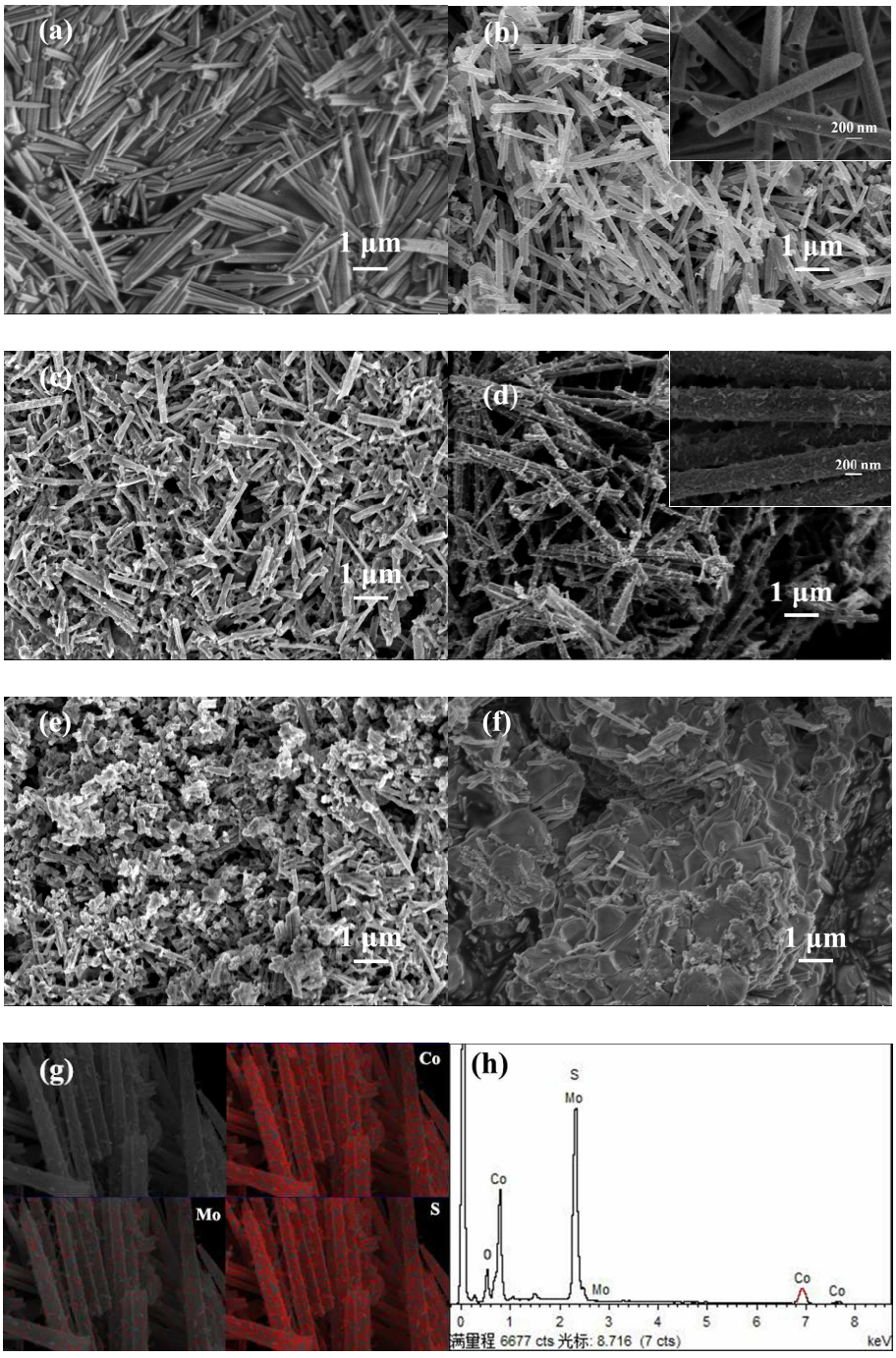

Fig. 3 FESEM images (a) $(Co(CO)_{0.35}Cl_{0.20}(OH)_{1.10}\cdot 1.74H_2O)$, (b) Co_9S_8, (c) $CoMoO_4/Co_9S_8$-40, (d) $CoMoO_4/Co_9S_8$-60 (e) $CoMoO_4/Co_9S_8$-80 (f) $CoMoO_4/Co_9S_8$-90 and (g) the element distribution mapping images of $CoMoO_4/Co_9S_8$-60, (h) the EDX spectroscopy of $CoMoO_4/Co_9S_8$-60.

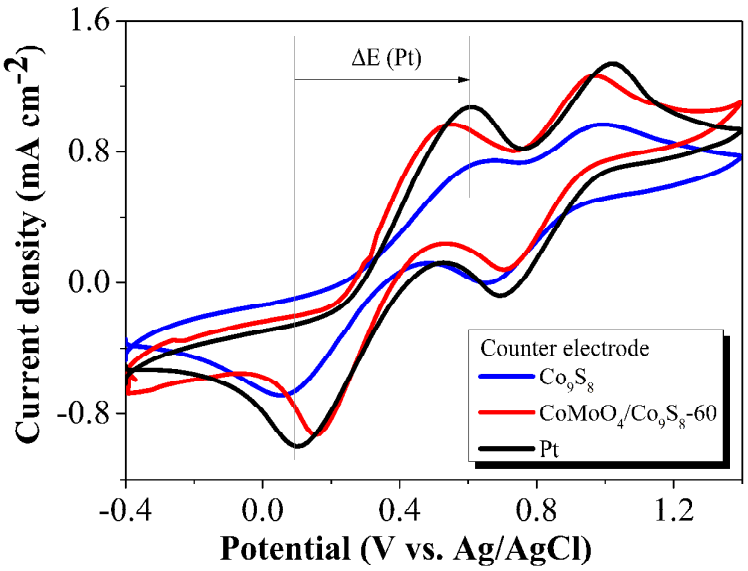

Fig. 4 CV curves of CEs: Co_9S_8, $CoMoO_4/Co_9S_8$-60 and Pt CEs at a scan rate of 50 mV s^{-1}.

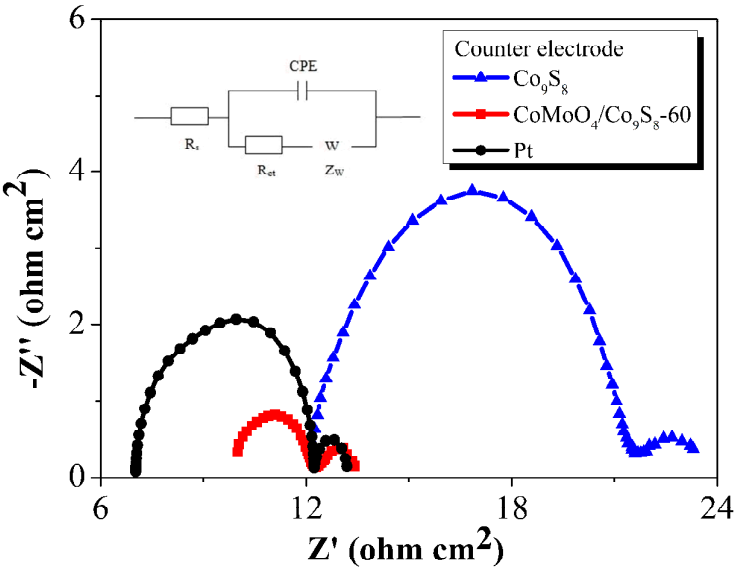

Fig. 5 EIS curves of Co_9S_8, $CoMoO_4/Co_9S_8$-60 and Pt CEs and the insert is the equivalent circuit diagram.

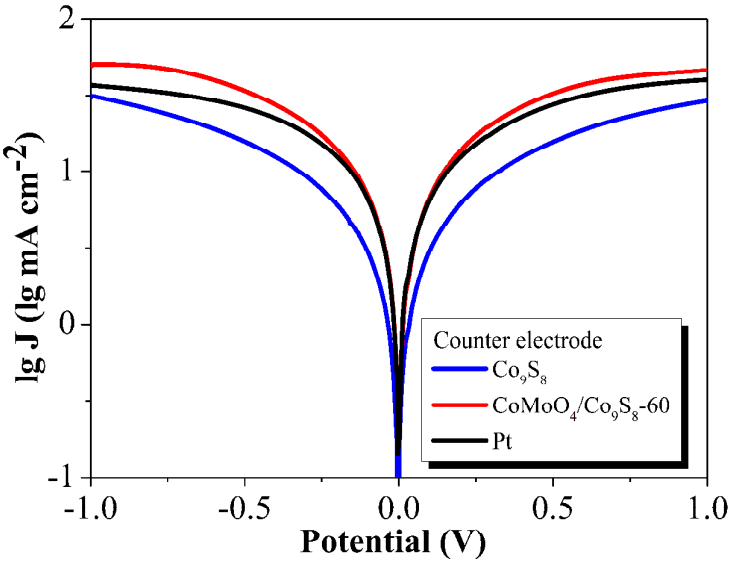

Fig. 6 Tafel curves of Co_9S_8, $CoMoO_4/Co_9S_8$-60 and Pt CEs.

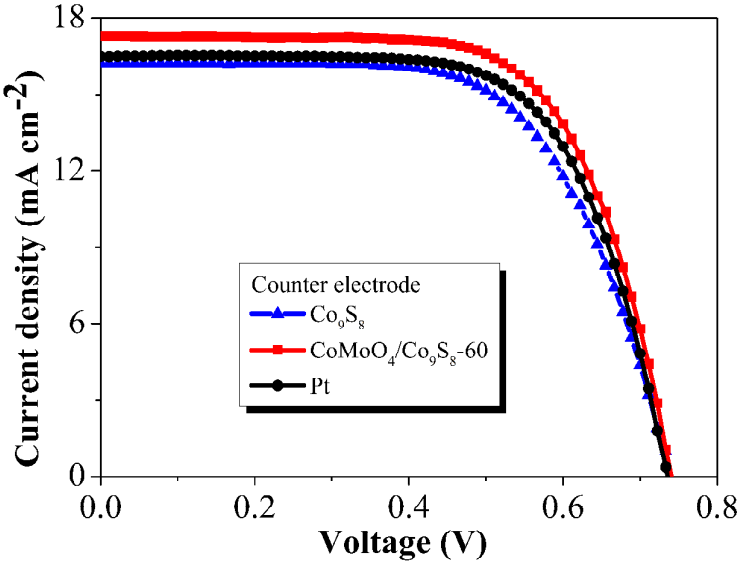

Fig. 7 J-V curves of the DSSCs based on Co_9S_8, $CoMoO_4/Co_9S_8$-60 and Pt CEs under the light intensity of 100 mW cm^{-2} (AM 1.5 G).

Table 1 CV and EIS data of Co_9S_8, $CoMoO_4/Co_9S_8$-60 and Pt CEs.

CE	ΔE (V)	J_{Red-1} (mA cm^{-2})	R_s (Ω cm^2)	R_{ct} (Ω cm^2)
Co_9S_8	0.612	0.688	12.17	9.52
$CoMoO_4/Co_9S_8$-60	0.402	0.931	10.00	2.29
Pt	0.504	1.002	7.03	5.21

Table 2 The photovoltaic data of the DSSCs based on Co_9S_8, $CoMoO_4/Co_9S_8$-60 and Pt CEs.

CE	V_{oc} (V)	J_{sc} (mA cm^{-2})	FF	PCE (%)
Co_9S_8	0.741	16.214	0.640	7.69
$CoMoO_4/Co_9S_8$-60	0.743	17.276	0.670	8.60
Pt	0.736	16.504	0.669	8.13